Fundamental Role of Oxygen Stoichiometry in Controlling the Band Gap and Reactivity of Cupric Oxide Nanosheets

Zachary S. Fishman,[†] Benjamin Rudshteyn,[‡] Yulian He,[§] Bolun Liu,[‖] Subhajyoti Chaudhuri,[‡] Mikhail Askerka,[‡] Gary L. Haller,[†,‡] Victor S. Batista,*[,‡] and Lisa D. Pfefferle*[,†]

[†]Department of Chemical and Environmental Engineering, Yale University, New Haven, Connecticut 06520-8286, United States
[‡]Department of Chemistry and Energy Sciences Institute, Yale University, New Haven, Connecticut 06520-8107, United States
[§]Department of Chemistry, Nankai University, Tianjin 300071, China
[‖]Department of Mechanical Engineering, Yale University, New Haven, Connecticut 06520-8286, United States

S *Supporting Information*

ABSTRACT: CuO is a nonhazardous, earth-abundant material that has exciting potential for use in solar cells, photocatalysis, and other optoelectronic applications. While progress has been made on the characterization of properties and reactivity of CuO, there remains significant controversy on how to control the precise band gap by tuning conditions of synthetic methods. Here, we combine experimental and theoretical methods to address the origin of the wide distribution of reported band gaps for CuO nanosheets. We establish reaction conditions to control the band gap and reactivity via a high-temperature treatment in an oxygen-rich environment. SEM, TEM, XRD, and BET physisorption reveals little to no change in nanostructure, crystal structure, or surface area. In contrast, UV−vis spectroscopy shows a modulation in the material band gap over a range of 330 meV. A similar trend is found in H_2 temperature-programmed reduction where peak H_2 consumption temperature decreases with treatment. Calculations of the density of states show that increasing the oxygen to copper coverage ratio of the surface accounts for most of the observed changes in the band gap. An oxygen exchange mechanism, supported by $^{18}O_2$ temperature-programmed oxidation, is proposed to be responsible for changes in the CuO nanosheet oxygen to copper stoichiometry. The changes induced by oxygen depletion/deposition serve to explain discrepancies in the band gap of CuO, as reported in the literature, as well as dramatic differences in catalytic performance.
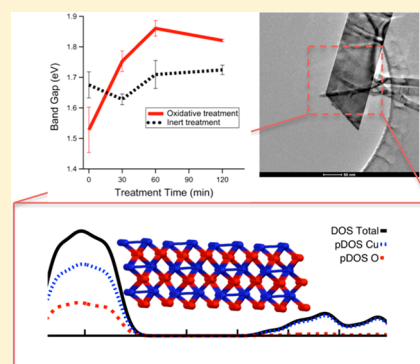
INTRODUCTION

In recent years much effort has gone toward raising the efficiencies of solar cells and photocatalytic processes. Researchers investigating materials such as GaAs, CdTe, InP, and others have shown results as good or better than their silicon counterparts.[1] The main limitation of silicon is its band gap, the minimum threshold energy a photon must possess before it can be absorbed, which placed at ∼1.07 eV causes it to miss long-wavelength light (>1100 nm).[2] Indeed, one reason these new materials work so well is because of their amenable band gap for solar light absorption according to the Shockley−Queisser limit.[3] The drawback, however, of many of these novel materials is their high toxicity and the fact that they contain rare-earth elements, which together serve to limit the sustainability of a device over its lifetime.[4] In the case of photocatalysis there are even more stringent constraints placed on a material; not only must its band gap be amenable to light absorption in the solar spectrum but also it must overcome the electrochemical barriers for a given reaction.[5] Other properties such as catalyst stability, toxicity, and abundance must also be considered.

Cupric oxide (CuO) is a p-type semiconductor that has been the subject of growing interest recently in the solar community as

well as other fields including batteries,[6] sensors,[7,8] catalysis,[9] supercapacitors,[10,11] and others. In solar cells, CuO nanorod arrays have been used as an anode with TiO_2,[12] as a barrier layer with ZnO,[13] and as an active layer with C_{60}.[14] Rajeshwar et al. found that differently synthesized CuO−Cu_2O nanorod arrays could photoelectrocatalytically convert CO_2 to methanol.[15] Though it was also found that the different synthesis conditions led to different efficiencies, it is still unclear what material properties led to these observed differences in performance.

Though much work has been done using CuO for specific applications, basic material properties remain poorly defined, most prominently band gap. The band gap of bulk copper oxide has been reported to be between 1.2 and 2.1 eV.[10,16−19] The band gap of nano-CuO has been reported to be as high as 4.03 eV.[20] Additional inconsistencies exist between experimental results and theoretical models as to whether the transition is direct or indirect. Many researchers have synthesized a wide range of CuO nanostructures through a variety of methods and noted how the band gap changes with different structures.[10] Though it is not
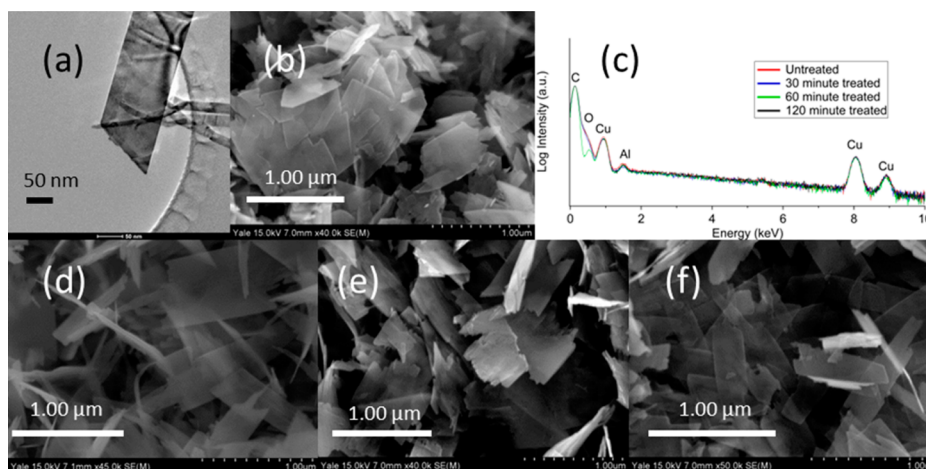
Figure 1. TEM (a) and SEM (b) images of untreated CuO nanosheets accompanied by EDX spectra (c) detailing its composition (copper and oxygen). The C and Al peaks are present because carbon tape was used to adhere powder samples to an aluminum stage. SEM images of 30, 60, and 120 min treated samples are presented in (d), (e), and (f), respectively.

unusual for band gap to change with nanosize and structure, this explanation alone does not sufficiently account for the wide range of band gaps reported in the CuO system. First, strong quantum confinement effects for CuO nanoparticles with crystallite sizes between 11 and 20 nm varied the band gap in a range of only 4.03−3.72 eV.[20] Second, the argument of different nanoshapes, rather than size, was shown only to vary the band gap in a range of 1.371−1.447 eV.[21] Third, large differences in band gap are reported even in the case of bulk (non-nano) CuO. This unexplained large variance in reported values suggests that the band gap of CuO may be highly susceptible to small material changes and therefore tunable.

2D CuO nanosheets were chosen for this study for multiple reasons: (1) CuO as a material has shown promise in a number of applications due to its low toxicity, high abundance, and good electrical and catalytic properties, etc. (2) A fundamental unanswered scientific question exists as to why CuO has such a large variation in reported band gaps even for the bulk. (3) Two-dimensional nanosheet structures are often more amenable to photocatalytic and solar cell applications because of their increased surface area, face-dependent activity and selectivity, more forgiving density of states, and ease of compositing through sheet−sheet stacking. Finally, while much research has been done on 0D and 1D there are only a few reports that discuss tuning the properties of 2D materials beyond graphene systems.[22,23]

In this work, CuO nanosheets were synthesized via a simple surfactant-assisted aqueous-phase method and then annealed at 350 °C in oxygen for different amounts of time. This annealing process was found to allow for the fine-tuning of the material's band gap as well as imbuing it with an increased reactivity. Theoretical tight-binding calculations show that oxygen coverage and arrangement strongly influence much of the band gap. A mechanism is finally proposed for this nondegradative process and supported with evidence from isotopic oxygen studies.

■ METHODS

Experimental Section. All chemicals used here were purchased from Sigma-Aldrich with purity ≥97%. All gases used were ultrahigh purity obtained from Airgas.

Synthesis of Cupric Oxide Nanosheets. Cupric oxide nanosheets were synthesized as per the following protocol:[39]

First, 120 g of sodium hydroxide and 22 g of hexadecyltrimethyl-ammonium bromide (CTAB) were dissolved in 900 mL of deionized water and heated to 60 °C under magnetic stirring. In a separate beaker, 3.4 g of copper(II) nitrate trihydrate was added to 100 mL of deionized water. Once dissolved the contents of the copper nitrate solution were added to the first solution such that the final concentrations of all species were 3 M NaOH, 60 mM CTAB, and 14 mM Cu(NO₃)₂, respectively. The solution was held at a constant temperature of 60 °C for 1 h and then removed from heating and filtered. The black precipitate was washed with excess deionized water and ethanol. To remove any remaining CTAB the samples were then calcined at 250 °C in air for 3 h and then finely ground with mortar and pestle before further treatment or characterization.

Oxidative and Inert Heat Treatment. The properties of cupric oxide nanosheets were tuned using a flow reactor as follows. Omega FMA-A2404, FMA-A2402-SS, and FMA5504 mass flow controllers were calibrated and used for all gas flow experiments. ColeParmer Digi-Sense R/S temperature controllers with Omega K-type thermocouples were calibrated and used for all temperature monitoring and controlling.

An appropriate amount of cupric oxide nanosheets (50−150 mg) was loaded into a straight quartz tube reactor and sealed within the setup. A stream of 100% oxygen was flowed over the sample at a rate of 100 mL/min. An hour was allowed for the flow to stabilize, after which point heating commenced. Under the previously mentioned gas flow conditions the sample was heated from room temperature to 100 °C over a period of 5 min and then heated from 100 to 350 °C over a period of 15 min. The sample was then left at 350 °C for a period of 30, 60, or 120 min depending on the treatment. After treatment, the sample was allowed to cool naturally under 100% oxygen flow and then subsequently removed for analysis.

Inert treatments were conducted under similar conditions except nitrogen was used as the flow gas instead of oxygen.

Scanning Electron Microscopy (SEM), Transmission Electron Microscopy (TEM), and Energy-Dispersive X-ray Spectroscopy (EDX). SEM images and TEM images were collected on a Hitachi SU-70 and FEI Tecnai Osiris, respectively, both equipped with an energy-dispersive X-ray detector. The acceleration voltage was 15 kV for SEM and 200 kV for TEM. For SEM, powder samples were pressed onto double-sided carbon tape, while TEM samples were dispersed in ethanol via sonication and then added dropwise to a holey carbon-coated gold grid. In both cases multiple spots were examined to ensure sample uniformity, and the EDX spectrum was acquired to verify that the structures were indeed composed of copper and oxygen.

X-ray Diffraction (XRD). XRD measurements were carried out on powder samples. Spectra were acquired from a Rigaku SmartLab X-ray diffractometer using Cu Kα radiation (λ = 1.5418 Å) with a rotating

anode source, operated at 45 kV and 200 mA. PDXL 2 Rigaku data analysis software was used to obtain lattice constants and crystallite sizes.

UV−Visible Spectroscopy (UV−vis). UV−vis spectra were collected from an Applied NanoFluorescence, LLC model NS1 Nanospectalyzer. Samples were sonicated in water until dispersed and then aliquoted into a 1 mL UV−visible transparent cuvette. Measurements were repeated three to five times per sample, and then a Tauc plot[24] was used to determine band gap. A software package was developed in house to automate this process as well as to improve interpretation consistency. The band gaps presented are the averages of the three to five samples, and the error bars represent the standard deviation of the measurements.

BET Surface Area. The surface area of CuO nanosheet samples was determined using a Quantachrome autosorb. Adsorption−desorption isotherms were constructed using an 11-point Brunauer, Emmett, and Teller (BET) measurements protocol with N_2 as the adsorbate. Typically 50−100 mg of sample was used and outgassed at 200 °C for 3−6 h. Measurements of each sample were performed in triplicate and their average and standard deviation calculated.

H_2 Temperature-Programmed Reduction (TPR) and $^{18}O_2$ Temperature-Programmed Oxidation (TPO). The TPR and isotopic oxygen studies were carried out in a reactor setup similar to that used for the O_2 treatments with the addition of a sampling line at the outlet leading to a vacuum chamber operating at 10^{-5} to 10^{-7} Torr containing a SRS RGA 100 residual gas analyzer which was used to perform real-time mass spectrometry measurements. For TPR, 50 mg of sample was loaded into a straight tube quartz reactor, and a gas stream composed of 10% H_2 gas (90% Argon) was flowed over it at a rate of 100 mL/min for 1 h prior to heating. Flow rates were controlled using mass flow controllers. Samples were then heated from room temperature to 100 °C in 5 min and then allowed to sit at 100 °C for 5 min before ramping from 100 to 400 °C at a rate of 10 °C per minute. For TPO, 50 mg of CuO nanosheets was loaded, and a gas stream composed of 4% $^{18}O_2$ (96% He) was flowed over the sample. The purity of the ^{18}O with respect to ^{16}O was reported as 99:1. The sample was then heated to 450 °C at a rate consistent with the TPR method. Again, the outlet gas was measured using the residual gas analyzer.

Computational. The structure of monoclinic CuO was generated from a unit cell found in the literature[25,26] with a = 18.612 Å, b = 13.640 Å, and c = 25.001 Å with α = 90.000°, β = 99.481°, and γ = 90.000°. The slab/supercell was generated by extending the structure along the (002) plane that was most expressed by the system (Figure 2). It contained 96
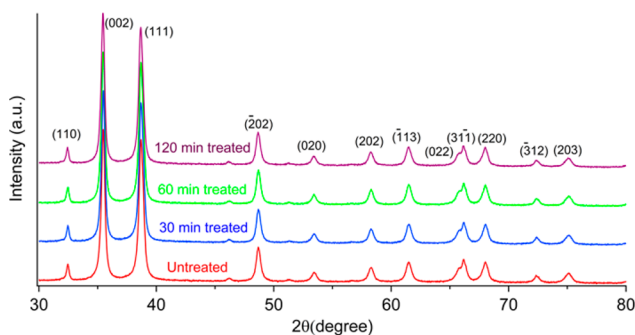

Figure 2. XRD spectra of CuO nanosheet 30 min (blue), 60 min (green), and 120 min (purple) treated and untreated (red) samples. Each peak is labeled with its corresponding face.

units of [CuO] with four alternating layers of 32 Cu and 32 O, resulting in a 6 Å thick slab. This structure is neutral, but each removed oxygen or copper atom increases the charge by 2 units or decreases the charge by 2 units, respectively. The long c lattice vectors act to install a spacer of about 17 Å to prevent unrealistic interactions between replicated slabs. The tight-binding extended Hückel[27−32] (EH) Hamiltonian (K = 1.75) was calculated using a locally modified version of YAeHMOP,[33] as described in our previous work.[34−39] The default YAeHMOP parameters developed by Hoffmann were used.[30,40] The calculation of the density of states of the slab in various states of Cu or O removal was

simulated with periodic boundary conditions at the Γ-point with Gaussian broadening with an exponent of 50, which is equivalent to a full width at half-maximum (fwhm) of 235 meV. The band gap was measured by taking the range of DOS intensities between the conduction and valence band edges where the intensities were less than 0.1 au.

The EH Hamiltonian was chosen for its ability to model efficiently very large structural models, with semiquantitative reliability using a minimal set of semiempirical parameters.[32,41−43] The method has already been extensively validated as applied to a wide range of semiconductor surfaces.[28,29,40,44,45] More recently Raza and co-workers[46−48] as well as our own group[34−39,41] have successfully demonstrated the capabilities of the EH Hamiltonian for understanding interfacial electron transfer on semiconductor surfaces. While the functional form of EH does not allow for geometry optimization,[49−52] it does allow for a complete treatment of orbital overlaps and the valence shell electronic structure. It performs well once supplied with the equilibrium geometry as described by crystallographic models or DFT methods,[32] as reported in this study. DFT calculations (SI, Section III) show minor surface reconstruction effects induced by changes in the level of oxygen coverage, providing robust structural models essential for an accurate description of changes in the band gap.

■ RESULTS AND DISCUSSION

Imaging. After synthesis, all samples were imaged to determine their nanostructure. Figures 1a and 1b show a typical TEM and SEM image (respectively) of an untreated sample. Here, we see that the material is in the form of nanosheets whose dimension ranges from 250 to 1000 nm in length and width. In previous work, we have found the nanosheet range in thickness between 15 and 25 nm.[53] Also of note is the nonuniformity in the edges of the nanosheets, which others have cited as a result of the nanosheet growth process.[10]

An EDX spectrum in Figure 1c provides elemental analysis of a structure found in the untreated sample and confirms it contains copper. Since carbon tape was used to adhere the sample to the stage and since this method is not sensitive enough to differentiate between the energies of carbon and oxygen, other methods (e.g., XRD) were used to confirm the material is in fact cupric oxide.

Figures 1d, 1e, and 1f show samples of copper oxide nanosheets after 30, 60, and 120 min of heat treatment at 350 °C, respectively. Here, we see that the nanosheet structure remains largely intact. Minor perturbations in the structure are, however, observable. For example, for the 120 min treated sample, there appears to be a rounding of the normally jagged edges present in the untreated sample. Indeed, for longer treatment times or for higher temperatures more extreme structural changes have been observed to occur (Figure S1). The temperature of 350 °C was chosen for this study because at higher temperatures structure loss was observed to occur too quickly.

Crystal Structure. X-ray diffraction (XRD) was used to determine the oxidation state and overall composition of the samples. Copper has two oxides: cuprous oxide (Cu_2O) with copper having a +1 oxidation state and cupric oxide (CuO) in which copper has a +2 oxidation state. Fortunately each of these oxidation states has exactly one associated crystal structure, which for cupric oxide is monoclinic. This makes XRD an ideal technique for differentiating between samples of cupric and cuprous oxide. Figure 2 shows XRD spectra collected for treated and untreated samples.

Peaks corresponding to each crystal face are labeled in Figure 2, and the lattice parameters of each are presented in Table 1. Lattice constants were found to be approximately 4.69, 3.43, and

Table 1. Lattice Parameters and Crystallite Sizes for the CuO Nanosheets in Figure 2

time treated (min)	a (Å)	b (Å)	c (Å)	β (deg)	crystallite size (Å)
untreated	4.6921	3.4287	5.1380	99.54	223 ± 28
30	6.6925	3.4275	5.1395	99.57	192 ± 62
60	4.6947	3.4276	5.1385	99.50	181 ± 51
120	4.6936	3.4218	5.1406	99.44	181 ± 56

5.14 Å for a, b, and c, respectively, and approximately 95° for β ($\alpha = \gamma = 90°$). The crystallite size was found to be approximately 200 Å which agrees with our previous studies[39] as well as empirical thickness calculations derived from surface area (see Reactivity section).

The lattice parameter values agree very well with literature values of CuO, and little change was observed for these values as a function of treatment time, which would suggest that the oxidative treatment has little to no effect on crystal structure or on the overall oxidation state. No cuprous oxide was detected in any sample.

Also of note is the increased amplitude of the peak associated with the (002) plane with respect to the other peaks compared to bulk (non-nano) CuO, which suggests an overexpression of the (002) plane in these CuO nanosheet samples, which other researchers have noted exhibits increased catalytic performance in the case of CO oxidation.[10,54] The high reactivity of this plane may leave it more susceptible to alterations such as by introducing or annealing away defects or by functionalization of its surface. Below, we will demonstrate how changes to the surface of CuO nanosheets lead to differences in optical properties and reactivity.

Optical Properties. UV–visible spectroscopy was used to test differences in the optical properties of the CuO nanosheet samples. This technique has been extensively implemented in semiconductor research to determine a material's band gap. Here, absorbance spectra of CuO nanosheets dispersed in deionized water were collected and plotted as a function of wavelength, which were then converted into Tauc plots[24] via the following transformation

$$(h\nu\alpha)^{1/n} = A(h\nu - E_g) \tag{1}$$

where h is Planck's constant; ν is the frequency of light; α is the absorption coefficient; n is $1/2$ for a direct band gap transition and 2 for an indirect band gap transition; A is a proportionality constant; and E_g is band gap. The band gap of a material may be determined by constructing a Tauc plot, that is by plotting $(\alpha E_{phot})^2$ against E_{phot}, where E_{phot} is the energy of a photon ($h\nu$). Linear extrapolation of each sample's trace down to the E_{phot} axis should yield the value of the band gap of the materials. Software was developed in house to automate this process and increase the consistency of the band gap determined for a given data set.

Example Tauc plots of each treatment are depicted in Figure S2, and calculated band gaps for each sample are plotted in Figure 3 as a function of treatment time. It was found that CuO nanosheets exhibit a direct band gap transition of 1.53 eV in the untreated sample. It was subsequently found that 30 min of oxidative treatment increased the band gap to 1.75 eV and 60 min to 1.86 eV. However, after 120 min of treatment, the band gap started to once again decrease, down to 1.82 eV. The standard deviations for all of these measurements were between 26 and 74 meV.
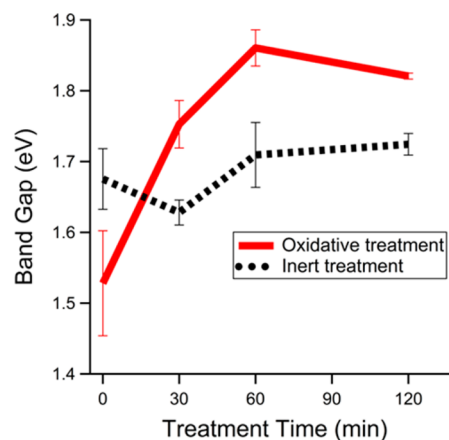

Figure 3. Band gaps of treated and untreated CuO nanosheet samples in an oxidative treatment (red solid) and with an inert treatment (black dotted). Each data point is an average over five measurements, and the error bars represent the standard deviation.

A separate sample of CuO nanosheets was treated at 350 °C for 30, 60, and 120 min in N_2 gas. Under these inert treatment conditions we observe a much smaller change in the band gap from 1.68 to 1.63 eV to 1.71 to 1.72 eV for untreated, 30, 60, and 120 min samples, respectively. We posit that the oxidative treatment results in more pronounced band gap changes due to increased O:Cu coverage of the CuO nanosheet surface. During inert treatment, no oxygen addition is possible from the gas phase though small band gap changes may be a result of oxygen and/or copper rearrangement from atoms already present on the surface. We also observe batch to batch differences in the band gap for untreated CuO nanosheets. In Figure 2, the untreated samples in the oxidative and inert series have a band gap of 1.53 and 1.68 eV, respectively, which we also attribute to a difference in the amount and distribution of surface oxygen atoms. Below, we use theoretical calculations in conjunction with experimental results to support these assertions as well as to demonstrate how differences to surface oxygen sites influence reducibility.

Theoretical Calculations. We have modeled the crystallographic structure of CuO, using tight-binding methods as described in the Computational methods section, to explore how the oxidative treatment changes the sample at a molecular level. Figure 4 shows the total density of states (DOS) for model 2D CuO nanosheets as well as the projected density of states (pDOS) for Cu and O atoms. For an ideal CuO structure with 1:1 ratio of Cu:O (Figure 4a), the band gap is 1.05 eV, in reasonable agreement with other theoretical calculations[55] and acceptably close to the band gap value found in Table 2 for the untreated sample. Typically, band gaps obtained at this level of theory underestimate the experimental band gaps by a few 100 meV.[55] To simulate an oxygen-rich surface, 8, 16, and 24 Cu atoms were removed from the top layer, as shown in Figures 4b, 4c, and 4d, respectively. Cu depletion resulted in a band gap increase, from 1.05 to 1.26 eV and 1.42 and 1.75 eV for the 0, 8, 16, and 24 Cu atoms removed, respectively. Conversely removing oxygen atoms from the bottom layer (Figure S3) resulted in a band gap decrease from 1.05 to 0.57 eV for 0 to 24 O atoms removed. These results are summarized in Table 3 and the Supporting Information. We find that changes in the band gap largely result from a change in the conduction band of the material, rich in Cu d states, increasing in the case of Cu removal and decreasing in the case of O removal. The results of our theoretical models are consistent with the experimental
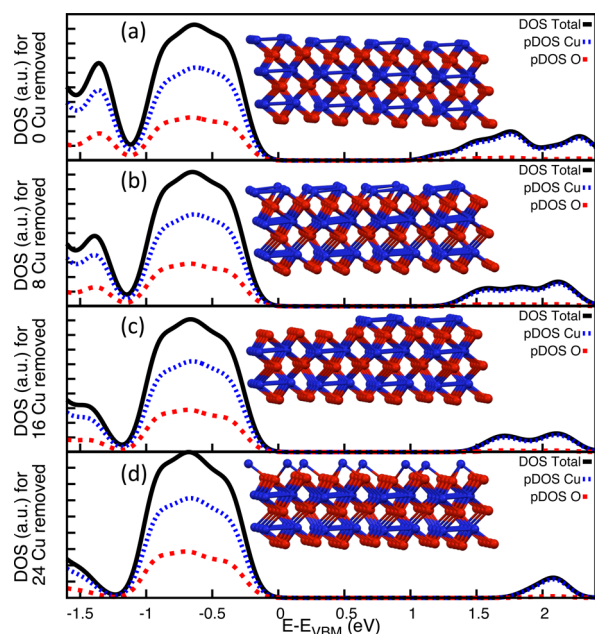
Figure 4. Total DOS (black) and pDOS (blue = Cu, red = O) for CuO (geometries shown as in insets) in various states of removal from the top copper layer in a "regular" fashion where the first atom is deleted in the first vertical row, the second atom is deleted in the second vertical row, etc. The pristine slab is given in (a). 8, 16, and 24 Cu atoms are deleted in (b), (c), and (d), respectively. Color code: blue = Cu, red = O. The energies are referenced to the valence band maximum.

Table 2. Mean Values for the Band Gap of Each CuO Nanosheet Sample

	band gap (eV)	
time treated (min)	oxidative	inert
untreated	1.53 ± 0.074	1.68 ± 0.043
30	1.75 ± 0.033	1.63 ± 0.018
60	1.86 ± 0.026	1.71 ± 0.046
120	1.82 ± 0.042	1.72 ± 0.015

Table 3. Values for the Band Gap of Each CuO Model Given in Figures 4 and 5

Cu atoms removed	arrangement	valence band (eV)	conduction band (eV)	band gap (eV)
0	regular	−11.4	−10.35	1.05
8	regular	−11.39	−10.13	1.26
16	regular	−11.38	−9.96	1.42
16	adjacent	−11.38	−10.22	1.16
16	alternating	−11.39	−9.72	1.67
16	areas	−11.38	−9.99	1.39
24	regular	−11.37	−9.62	1.75

conclusion that the band gap of CuO increases with increasing surface oxygen coverage. It is expected that the surface of CuO nanosheets becomes relatively more oxygen rich when exposed to the oxidative treatment, which is consistent with the observed increase in band gap. Similar results were obtained for CuO nanowires where adsorption of water to the (111) surface resulted in a wider band gap.[56]

The rearrangement of oxygen on the surface was also investigated using molecular modeling to determine its impact on the CuO nanosheet band gap. Such calculations effectively model the effect of surface rearrangement upon oxidation or

reduction. In Figure 5a, 16 Cu atoms were removed from the bottom layer, but the pattern of removal was varied. In Figure 5a,
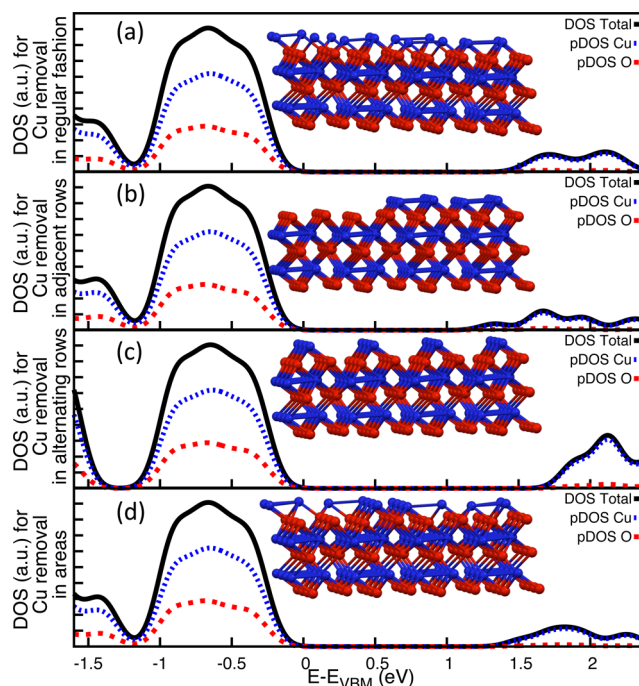

Figure 5. Total DOS (black) and pDOS (blue = Cu, red = O) for CuO (geometries shown as in insets) in various states of removal of 16 Cu atoms from the top layer. For the "regular fashion" pattern of removal (a) the first atom of the first vertical row was deleted, the second atom of the second row, etc. In (b) adjacent rows of Cu atoms were deleted. In (c) alternating rows were deleted. "Areas" (d) refer to roughly hexagonal portions deleted from the surface. Color code: blue = Cu, red = O. The energies are referenced to the valence band maximum.

the atoms were removed in a regular fashion, that is, the first Cu atom of the first row, the second Cu atom of the second row, etc. which was also the method of removal in Figure 4. For comparison, the adjacent rows of Cu atoms were removed (Figure 5b) resulting in a band gap of 1.16 eV. In Figure 5c, alternative rows were removed resulting in a band gap of 1.67 eV. In Figure 5d, hexagonal areas of Cu atoms were removed yielding a band gap of 1.39 eV. The structures used are displayed in the inset of each DOS plot. Analogous plots with oxygen atoms removed can be found in Figure S4. These results are also summarized in Table 3 and Table S1. Diffuse removal of Cu atoms such as in (a) or (d) yielded structures with very similar band gaps, while more ordered removal patterns such as those found in (b) and (c) resulted in band gaps that were much more varied. We posit that by removing atoms in such a clustered configuration a new interface is created between two separate materials. These metal−metal oxide interfaces could provide a collection of mid band gap of energy states in between the more populated band edges, hence lowering the apparent band gap of the material. We selected to remove 16 Cu atoms to test arrangement effects because it results in a Cu:O ratio of 1:1.20 which, as will be shown below, is close to the ratio measured experimentally for CuO nanosheets.

These theoretical results also help explain changes found in CuO nanosheets treated in an inert environment. Slight increases and decreases in band gap found can be attributed to the rearrangement of oxygen atoms on the surface. For example, structures may transition from a "regular" distribution to an

"alternating" arrangement, which would increase the band gap, then to an "adjacent" configuration, which would decrease the band gap, or to the "areas" structure, which would keep the band gap relatively constant. Based on the experimental results the latter is more likely since little to no change in band gap is observed.

Reactivity. In this section, we demonstrate how increases in the band gap of CuO nanosheets correlate with increases in reactivity. Hydrogen oxidation was used as a probe reaction to quantify differences in reducibility. The reduction of CuO in hydrogen gas is a well-studied process.[42] CuO, rather than being reduced sequentially to Cu_2O and then to Cu, has been shown to reduce directly to Cu according to the following reaction

$$CuO(s) + H_2(g) \rightarrow Cu(s) + H_2O(g)$$
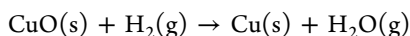
First, the surface areas of all samples were measured in triplicate using 11 point BET N_2 physisorption. The mean of each sample along with the standard deviation is listed in Table 4. All samples

Table 4. Mean Surface Area Values and Estimated Nanosheet Thicknesses for Each CuO Sample Are Presented

time treated (min)	surface area (m^2/g)	average calculated thickness (nm)
untreated	23.05 ± 0.66	13.75
30	20.79 ± 1.84	15.25
60	21.89 ± 0.41	14.48
120	21.87 ± 1.06	14.49

fell within a range of 20−24 m^2/g with very little difference in surface area between them. Interestingly, surface area can be used to calculate the average thickness of the nanosheets present within the sample using eq 2.

$$\bar{t} = \frac{2}{\sigma\rho} \tag{2}$$

where $\bar{t}$ is the average thickness of a CuO nanosheet; σ is the surface area per unit mass of the sample; and ρ is the density of CuO, which is 6.31×10^6 g/m^3. An analogue analysis is done by Weiber et al. for 0D nanoparticles;[57] however, since no such report exists for 2D materials (to the best of our knowledge) a short derivation is included in the Supporting Information, Section II.

Thicknesses for each sample are presented in Table 4. These values are likely an underestimation of the actual thickness since roughness and jagged edges, which are visible from the SEM images in Figure 1, increase the surface area. Interestingly these values are in agreement with crystallite sizes obtained from XRD. Together with the SEM images shown in Figure 1, these data reinforce the claim that the treatment has not impacted the structure of the CuO nanosheets

H_2 TPR was performed on oxidized CuO nanosheets, as shown in Figure 6. Here 50 mg of treated and untreated samples were heated in 10% H_2 gas (in an Ar atmosphere) flow from 100 to 400 °C, and the composition of the outlet gas stream was assessed using mass spectrometry. Since no gaseous oxygen is present for this reaction, all hydrogen that is consumed is being oxidized by the CuO nanosheets, which degrades the CuO nanosheets so that neither structure nor composition is preserved. However, differences in the initial state of the nanosheets affect the temperature at which the material reacts.

Percent H_2 consumption is given as a function of temperature in Figure 6 for each sample. At a given temperature, increased H_2 consumption indicates more reaction is occurring between the
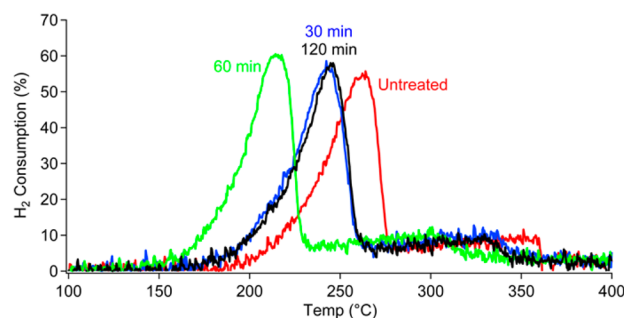

Figure 6. Mass spectrum-derived percent consumption of H_2 for 50 mg of each sample at different temperatures with tabular values given in Table 5.

material and the gas. When all of the oxygen has been depleted (i.e., when all CuO has been converted to Cu) the reaction ceases, and no further H_2 is consumed. In Figure 6, we see that peak H_2 consumption temperature decreases from 261 °C for the untreated sample to 242 °C for the 30 min treated sample and to 214 °C for the 60 min sample. For the 120 min sample, the peak H_2 consumption temperature increases back to 244 °C. Note that this follows a similar trend to the sample's band gap in that CuO nanosheets with higher band gap show increased reactivity with H_2 (as indicated by a lower reaction temperature) and vice versa, which indicates that there is a correlation between the band gap and reactivity of CuO nanosheets so that by tuning one the other is also tuned, which makes it possible to predict *a priori* how changes in the band gap of CuO nanosheets will impact its reactivity.

Values for total H_2 consumed are listed in Table 5. These values were derived by integrating the H_2 consumption curves

Table 5. Peak Consumption Temperatures[a]

time treated (min)	peak H_2 consumption temp. (°C)	total H_2 consumed (mmol)	Cu:O
untreated	261	0.794	1:1.26
30	242	0.761	1:1.21
60	214	0.777	1:1.23
120	244	0.775	1:1.24

[a]These temperatures follow a trend similar to the material band gap. Total H_2 consumed was found by integrating each peak and using the ideal gas law. Cu:O ratios were determined assuming 1 mol of H_2 per atom of O present in the material.

and using the prior knowledge of the quantity of H_2 flowed during the experiment. Equation 3 outlines this explicitly.

$$\frac{\text{Peak Area}}{\text{Total Area}} = \frac{H_2 \text{ Consumed}}{\text{Total } H_2 \text{ Flowed}} \tag{3}$$

where Total Area is the area below the line $y = 100\%$ from 100 to 400 °C or 100*300 = 30 000 which is the theoretical maximum consumption. The total H_2 flowed refers the total amount of moles calculated using a flow rate of 10 mL/min (10% of a 100 mL/min stream) and the ideal gas law. From the above reaction, 1 molecule of H_2 is consumed per oxygen atom of CuO. Therefore, these values also serve as a measure of oxygen content for these structures. The theoretical amount of O atoms in 50 mg of sample with a 1:1 Cu:O ratio is 0.630 mmol. In this study we find that all CuO nanosheet samples had increased amounts of oxygen. As depicted in Table 4 the Cu:O ratio goes from 1:1.26 in the untreated sample to 1:1.21 to 1:1.24 to 1:23. Thus, all CuO

nanosheets studied here have an excess amount of oxygen, which would explain why the band gaps do not match a theoretical pristine slab of CuO where the ratio for Cu:O is 1:1. This trend is not identical to the trend in band gap in that the untreated sample, though it contains the most oxygen, does not have the highest band gap. In the treated samples, however, the oxygen amount does follow the trend of band gap. Based on our theoretical calculations, we conclude that the surface oxygen atoms in the untreated sample are more dispersed than the treated samples, which corroborates the hypothesis made in the previous section that the solution synthesized CuO nanosheets exist in a different configuration, and with heat treatment these structures can rearrange, changing their band gap. More robust spectroscopic methods may reveal that the surface of untreated CuO nanosheets contains more hydroxyl groups that likely affect the band gap in different ways, as suggested in the literature,[58,59] which is beyond the scope of this investigation.

H_2 TPR was also performed on a commercial sample of CuO, and it was found that it contained only 3.9% more oxygen (Figure S5). The high surface-to-bulk ratio of CuO nanosheets suggests that a large amount of additional oxygen lies on the surface of the material, which would explain why the band gaps reported in this work are slightly higher than the most commonly cited value of 1.4 eV.

To further support the hypothesis that oxygen from the gas phase is interacting with the material and vice versa, ^{18}O temperature-programmed oxidation was performed on untreated CuO nanosheets. Figure 7 shows the production of $^{18,16}O_2$ as a function of temperature over untreated CuO nanosheets in the presence of ^{18}O.
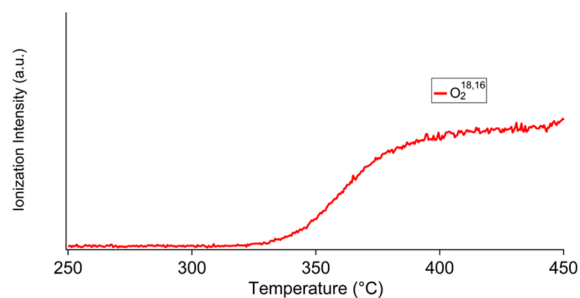

Figure 7. Mass spectrum of $^{18,16}O_2$ for the reaction of CuO nanosheets (untreated) heated in the presence of isotopic oxygen gas ($^{18}O_2$).

At approximately 325 °C there is an onset of production of $^{18,16}O_2$. Since the atmosphere is the only source of ^{18}O atoms (in the form of $^{18}O_2$) and CuO nanosheets are the only source of ^{16}O atoms, the production of $^{18,16}O_2$ molecules must be a result of oxygen exchange occurring between the nanosheets and the gas. This mechanism similar to Mars−Van Krevelin catalysts[60] is indicative of increased oxygen mobility in the material. We posit that this phenomenon might also be the mechanism of structural degradation in nanosheet samples heated over long time periods around this temperature (Figure S1). Thus, we conclude that the band gap and reactivity changes are a direct result of this oxygen mobility and exchange.

In analogous systems, such as carbon nanotubes, surface oxygen groups impact properties such as toxicity, reactivity, and point of zero charge.[61] Additionally, others have noted the correlation between band gap and catalytic performance in metal oxide systems.[62] Here, we find that the total amount of surface oxygen as well as its distribution affect the band gap and

hydrogen oxidation activity of CuO nanosheets. We also find that these optical and catalytic properties may be tuned through varying the calcination condition.

CONCLUSIONS

We have elucidated the fundamental role that surface oxygen deposition plays in tuning the band gap and reactivity of CuO nanosheets, an earth-abundant, nonhazardous material, useful in the fields of solar energy technology and photocatalysis. We demonstrated that the band gap of CuO nanosheets can be controlled in a range of 1.53−1.86 eV through a mild oxidative heat treatment. We found that the reactivity of the nanosheets improves upon increasing the band gap, as evidenced by H_2 TPR. The observed changes in band gap and reactivity are directly correlated with changes in surface oxygen coverage, as supported by our theoretical analysis. Calculations of the DOS for a series of model CuO nanosheets show that structures with increased surface oxygen atoms have larger band gaps. Additionally, the band gaps of models with more ordered arrangements varied widely from those of more diffuse arrangements. Finally, through isotopic oxygen TPO, we demonstrate that oxygen exchange is indeed occurring between the gas phase and the solid during the oxidative heat treatments at 350 °C. We hypothesize that the sensitivity to surface oxygen vacancies is an important contributing factor for the wide range of values of CuO band gaps reported in the literature.

ASSOCIATED CONTENT

ⓈSupporting Information

The Supporting Information is available free of charge on the ACS Publications website at DOI: 10.1021/jacs.6b05332.

> SEM image showing the effects that long heat treatments have on CuO nanosheets, namely, that nanostructure degradation begins with the smoothing of the material's jagged edges, mass spectrometry data for H_2 TPR of commercial CuO showing the percent of H_2 consumed at any given temperature, derivation of eq 2, and coordinates for structures used for the theoretical calculations (PDF)

AUTHOR INFORMATION

Corresponding Authors
*victor.batista@yale.edu
*lisa.pfefferle@yale.edu
Notes
The authors declare no competing financial interest.

ACKNOWLEDGMENTS

■ REFERENCES

(1) Green, M. A.; Emery, K.; Hishikawa, Y.; Warta, W.; Dunlop, E. D. *Prog. Photovoltaics* **2015**, *23*, 1.

(2) Wu, C.; Crouch, C. H.; Zhao, L.; Carey, J. E.; Younkin, R.; Levinson, J. A.; Mazur, E.; Farrell, R. M.; Gothoskar, P.; Karger, A. *Appl. Phys. Lett.* **2001**, *78*, 1850.

(3) Shockley, W.; Queisser, H. J. *J. Appl. Phys.* **1961**, *32*, 510.

(4) Hardman, R. *Environ. Health Perspect.* **2006**, *114*, 165.

(5) Rajeshwar, K. In *Encyclopedia of Electrochemistry*; Wiley-VCH Verlag GmbH & Co. KGaA: 2007.

(6) Gao, X.; Bao, J.; Pan, G.; Zhu, H.; Huang, P.; Wu, F.; Song, D. *J. Phys. Chem. B* **2004**, *108*, 5547.

(7) Chen, W.; Chen, J.; Feng, Y.-B.; Hong, L.; Chen, Q.-Y.; Wu, L.-F.; Lin, X.-H.; Xia, X.-H. *Analyst* **2012**, *137*, 1706.

(8) Song, J.; Xu, L.; Zhou, C.; Xing, R.; Dai, Q.; Liu, D.; Song, H. *ACS Appl. Mater. Interfaces* **2013**, *5*, 12928.

(9) Dow, W.-P.; Wang, Y.-P.; Huang, T.-J. *J. Catal.* **1996**, *160*, 155.

(10) Zhang, Q.; Zhang, K.; Xu, D.; Yang, G.; Huang, H.; Nie, F.; Liu, C.; Yang, S. *Prog. Mater. Sci.* **2014**, *60*, 208.

(11) Zhang, X.; Shi, W.; Zhu, J.; Kharistal, D. J.; Zhao, W.; Lalia, B. S.; Hng, H. H.; Yan, Q. *ACS Nano* **2011**, *5*, 2013.

(12) Anandan, S.; Wen, X.; Yang, S. *Mater. Chem. Phys.* **2005**, *93*, 35.

(13) Raksa, P.; Nilphai, S.; Gardchareon, A.; Choopun, S. *Thin Solid Films* **2009**, *517*, 4741.

(14) Sun, S.; Zhang, X.; Zhang, J.; Wang, L.; Song, X.; Yang, Z. *CrystEngComm* **2013**, *15*, 867.

(15) Rajeshwar, K.; de Tacconi, N. R.; Ghadimkhani, G.; Chanmanee, W.; Janáky, C. *ChemPhysChem* **2013**, *14*, 2251.

(16) Marabelli, F.; Parravicini, G.; Salghetti-Drioli, F. *Phys. Rev. B: Condens. Matter Mater. Phys.* **1995**, *52*, 1433.

(17) Ogwu, A.; Darma, T.; Bouquerel, E. *J. Achiev. Mater. Manuf. Eng.* **2007**, *24*, 172.

(18) Ray, S. C. *Sol. Energy Mater. Sol. Cells* **2001**, *68*, 307.

(19) Hardee, K. L.; Bard, A. J. *J. Electrochem. Soc.* **1977**, *124*, 215.

(20) Rehman, S.; Mumtaz, A.; Hasanain, S. *J. Nanopart. Res.* **2011**, *13*, 2497.

(21) Yang, M.; He, J. *J. Colloid Interface Sci.* **2011**, *355*, 15.

(22) Chhowalla, M.; Shin, H. S.; Eda, G.; Li, L.-J.; Loh, K. P.; Zhang, H. *Nat. Chem.* **2013**, *5*, 263.

(23) Lee, H. S.; Min, S.-W.; Chang, Y.-G.; Park, M. K.; Nam, T.; Kim, H.; Kim, J. H.; Ryu, S.; Im, S. *Nano Lett.* **2012**, *12*, 3695.

(24) Tauc, J.; Grigorovici, R.; Vancu, A. *Phys. Status Solidi B* **1966**, *15*, 627.

(25) Villars, P. CuO Crystal Structure Inorganic Solid Phases 2014. http://materials.springer.com/isp/crystallographic/docs/sd_0542121 (accessed April 11, 2016).

(26) Tunell, G.; Posnjak, E.; Ksanda, C. Z. *Kristallogr. - Cryst. Mater.* **1935**, *90*, 120.

(27) Wolfsberg, M.; Helmholz, L. *J. Chem. Phys.* **1952**, *20*, 837.

(28) Hoffmann, R. *J. Chem. Phys.* **1963**, *39*, 1397.

(29) Hoffmann, R. *Solids and surfaces: a chemist's view of bonding in extended structures*; VCH Publishers: New York, 1988.

(30) Alvarez, S. *Tables of parameters for extended Hückel calculations* **1989**.

(31) Burdett, J. K. *Chemical Bonding in Solids*; Oxford University Press, 1995.

(32) Lewars, E. G. *Computational chemistry: introduction to the theory and applications of molecular and quantum mechanics*; Springer Science & Business Media, 2010.

(33) Landrum, G.; Glassey, W.; *Yet Another Extended Hückel Molecular Orbital Package (YAeHMOP)*; 3.0 ed.; Cornell University: 2001.

(34) Rego, L. G.; Batista, V. S. *J. Am. Chem. Soc.* **2003**, *125*, 7989.

(35) Abuabara, S. G.; Rego, L. G.; Batista, V. S. *J. Am. Chem. Soc.* **2005**, *127*, 18234.

(36) Abuabara, S. G.; Cady, C. W.; Baxter, J. B.; Schmuttenmaer, C. A.; Crabtree, R. H.; Brudvig, G. W.; Batista, V. S. *J. Phys. Chem. C* **2007**, *111*, 11982.

(37) McNamara, W. R.; Snoeberger III, R. C.; Li, G.; Schleicher, J. M.; Cady, C. W.; Poyatos, M.; Schmuttenmaer, C. A.; Crabtree, R. H.; Brudvig, G. W.; Batista, V. S. *J. Am. Chem. Soc.* **2008**, *130*, 14329.

(38) Rego, L. G.; Silva, R. d.; Freire, J. A.; Snoeberger, R. C.; Batista, V. S. *J. Phys. Chem. C* **2009**, *114*, 1317.

(39) Li, C.; Koenigsmann, C.; Ding, W.; Rudshteyn, B.; Yang, K. R.; Regan, K. P.; Konezny, S. J.; Batista, V. S.; Brudvig, G. W.; Schmuttenmaer, C. A.; et al. *J. Am. Chem. Soc.* **2015**, *137*, 1520.

(40) Hoffmann, R. *Rev. Mod. Phys.* **1988**, *60*, 601.

(41) Rego, L. G.; Abuabara, S. G.; Batista, V. S. *J. Chem. Phys.* **2005**, *122*, 154709.

(42) Cerda, J.; Soria, F. *Phys. Rev. B: Condens. Matter Mater. Phys.* **2000**, *61*, 7965.

(43) MacGlynn, S. P.; Vanquickenborne, L. G.; Kinoshita, M.; Carroll, D. G. *Introduction to Applied Quantum Chemistry*; Holt Rinehart & Winston: New York, 1972.

(44) Hay, P. J.; Thibeault, J. C.; Hoffmann, R. *J. Am. Chem. Soc.* **1975**, *97*, 4884.

(45) Hoffmann, R. *Angew. Chem., Int. Ed. Engl.* **1987**, *26*, 846.

(46) Raza, H. *Phys. Rev. B: Condens. Matter Mater. Phys.* **2007**, *76*, 045308.

(47) Raza, H.; Bevan, K. H.; Kienle, D. *Phys. Rev. B: Condens. Matter Mater. Phys.* **2008**, *77*, 035432.

(48) Raza, H.; Kan, E. C. *J. Comput. Electron.* **2008**, *7*, 372.

(49) Jug, K. *Theor. Chim. Acta* **1980**, *54*, 263.

(50) Levine, I. N. *Quantum Chemistry*; Pearson Prentice Hall, 2009.

(51) Perdew, J. P. *Int. J. Quantum Chem.* **1985**, *28*, 497.

(52) Heinemann, M.; Eifert, B.; Heiliger, C. *Phys. Rev. B: Condens. Matter Mater. Phys.* **2013**, *87*, 115111.

(53) Gilbertson, L. M.; Albalghiti, E. M.; Fishman, Z. S.; Perreault, F.; Corredor, C.; Posner, J. D.; Elimelech, M.; Pfefferle, L. D.; Zimmerman, J. B. *Environ. Sci. Technol.* **2016**, *50*, 3975.

(54) Huang, H.; Zhang, L.; Wu, K.; Yu, Q.; Chen, R.; Yang, H.; Peng, X.; Ye, Z. *Nanoscale* **2012**, *4*, 7832.

(55) Ghijsen, J.; Tjeng, L.; Van Elp, J.; Eskes, H.; Westerink, J.; Sawatzky, G.; Czyzyk, M. *Phys. Rev. B: Condens. Matter Mater. Phys.* **1988**, *38*, 11322.

(56) Hu, J.; Li, D.; Lu, J. G.; Wu, R. *J. Phys. Chem. C* **2010**, *114*, 17120.

(57) Weibel, A.; Bouchet, R.; Boulc', F.; Knauth, P. *Chem. Mater.* **2005**, *17*, 2378.

(58) Warren, S.; Flavell, W.; Thomas, A.; Hollingworth, J.; Dunwoody, P.; Downes, S.; Chen, C. *Surf. Sci.* **1999**, *436*, 1.

(59) Takita, Y.; Saito, Y.; Tashiro, T.; Hori, F. *Bull. Chem. Soc. Jpn.* **1985**, *58*, 1827.

(60) Doornkamp, C.; Ponec, V. *J. Mol. Catal. A: Chem.* **2000**, *162*, 19.

(61) Gilbertson, L. M.; Goodwin, D. G., Jr; Taylor, A. D.; Pfefferle, L.; Zimmerman, J. B. *Environ. Sci. Technol.* **2014**, *48*, 5938.

(62) Getsoian, A. B.; Zhai, Z.; Bell, A. T. *J. Am. Chem. Soc.* **2014**, *136*, 13684.